energies

MDPI

Article

Innovations in Passive Downdraft Cooling Performance Evaluation Methods: Design and Construction of a Novel Environmental Test Chamber

Omar Dhia Al-Hassawi * and David Drake

School of Design and Construction, Washington State University, Carpenter Hall 114, Pullman, WA 99164, USA
* Correspondence: omar.al-hassawi@wsu.edu; Tel.: +1-(480)-406-3419

Abstract: Energy demand for active mechanical space cooling is projected to double by 2050. Wider adoption of passive cooling systems can help reduce demand. However, familiarity with these systems remains low, and innovation in the field is constrained due to a lack of cost-effective, accessible performance evaluation methods. This paper reports the design, construction, and commissioning of an affordable, self-contained environmental test chamber. The novel chamber replicates a range of outdoor conditions common in hot, dry regions, making possible year-round testing of reduced-scale prototypes. Data from calibration testing are reported, showing no significant difference in evaporative efficiency when a reduced-scale prototype tested in the chamber is compared with datasets from prior full-scale testing. Analyzing the results using an independent sample two-tailed t-test with a 95% confidence interval found a p-value of 0.75. While measured outlet air velocities for reduced-scale and full-scale prototypes differed to some extent (root mean square error of 0.45 m/s), results were nevertheless deemed comparable due to errors introduced by the rapid change in wind speeds and directions at full scale. Future chamber modifications will correct misalignments between data collected from the two scales and prevent observed increases in the chamber's relative humidity levels during testing.

Keywords: passive downdraft cooling; passive downdraft evaporative cooling towers; passive cooling; environmental test chamber; prototype testing

Citation: Al-Hassawi, O.D.; Drake, D. Innovations in Passive Downdraft Cooling Performance Evaluation Methods: Design and Construction of a Novel Environmental Test Chamber. *Energies* **2023**, *16*, 4371. https://doi.org/10.3390/en16114371

Academic Editors: Jarek Kurnitski, John Gardner, Seongjin Lee, Kee Han Kim and Sukjoon Oh

Received: 10 March 2023
Revised: 15 May 2023
Accepted: 26 May 2023
Published: 27 May 2023

1. Introduction

Globally, buildings consume 60 percent of available electricity, 18 percent of which is due to space cooling. Barring an alternative, electricity demand for space cooling is projected to double by 2050, driven by accelerating urbanization, primarily in hot and warm climates [1,2]. This adds additional loads on the electric grid during peak use periods. To the extent the electricity to satisfy these demands is generated by nonrenewable means, increased mechanical space cooling results in an increase in carbon emissions, exacerbating the demand for cooling in the future.

Meeting space cooling loads with passive systems rather than active mechanical air conditioning systems can play two important roles. The first is reducing burdens on electrical grids, and the second is reducing or eliminating carbon emissions associated with energy generation due to the increased use of active mechanical cooling. However, this will require wider adoption of passive systems than is currently the case.

The basic principles of passive cooling have been understood and applied since ancient times, and there have been continuous innovations in the field, resulting in contemporary passive systems that are not only effective, but capable of being integrated into commercial and residential buildings. In spite of this, applications for passive cooling systems remain limited, due to widespread unfamiliarity with the systems and consequent misperceptions regarding their performance and operation.

1.1. Passive Cooling Principles

Effective passive cooling requires limiting space heat gains, then modulating any unavoidable gains, and finally dissipating sensible and latent heat gains without reliance on mechanical systems using three heat sinks: the atmosphere, the sky, and the earth [3,4]. Cross and stack ventilation, wind towers, and downdraft evaporative cooling towers dissipate heat into the atmosphere through convection and evaporation. Roof ponds transfer heat into the night sky through radiation, and earth tubes as well as earth contact exchange heat with the ground through conduction [5].

1.2. Passive Downdraft Cooling Systems in Buildings

Heat transfer through direct evaporation of water is one of the oldest means of passive cooling, dating back to ancient Egypt around 2500 B.C. and then evolving to be integrated with the outlets of wind towers in the desert regions of Iran in the early tenth century [6]. Innovations in wind tower design came in the 1980s when a rigid media direct evaporative cooling system was placed at the top of the tower, causing heavier, cooler air to drop downwards by gravity; hence, the design was named the passive downdraft evaporative cooling tower (PDECT) [7].

PDECT designs were subsequently refined through variations to the tower inlet cooling mechanisms which can be classified under three categories illustrated in Figure 1. The first is direct or latent cooling which uses rigid media, shower heads, or misting nozzles. The second is indirect or sensible cooling which uses closed-loop chilled water pipes. The third is hybrid cooling which uses a combination of direct and indirect cooling [8].

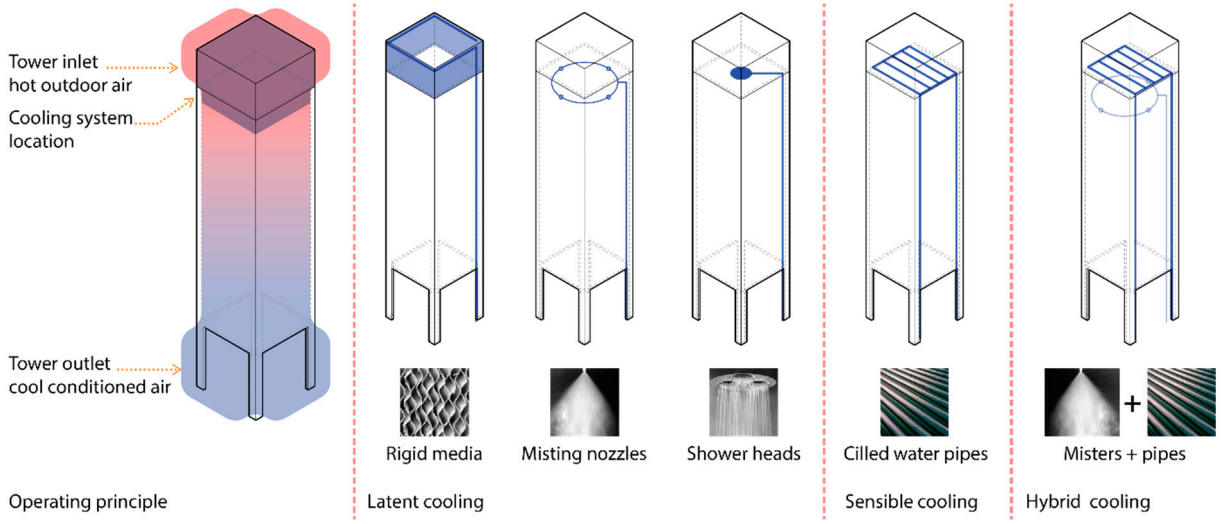

Figure 1. PDECT operational principle and cooling mechanisms.

Studies have demonstrated that built PDECT examples are energy- and water-efficient, cost-effective, and thermally comfortable under most conditions [9]. This is in contrast to widespread misperceptions regarding PDC performance and operation, and risk-averse reliance on more familiar active AC systems.

In the United States, more than 88 percent of residential building stock uses mechanical air conditioning systems for space cooling [10]. Because mechanical AC systems are designed to maintain interior temperatures and relative humidity within very narrow ranges, a barrier to wider adoption of PDC systems may be the assumption that occupant comfort requires precise control beyond the performance capabilities of passive systems, and that passive downdraft cooling is incapable of providing reliable thermal comfort for occupants.

Most PDC systems use direct latent cooling, leading to the misperception that passive systems use substantially more water during their operation than comparable mechanical

AC systems. This is also a barrier to PDC adoption, particularly in hot dry regions with limited water supplies. In fact, PDC has proven to be a competitive solution when water used in the generation of electricity to power mechanical AC systems is included [11].

1.3. Passive Downdraft Cooling System Performance Evaluation Methods

While effective research methods exist for evaluating the performance of PDC systems, most of these methods require considerable investments in terms of space, capital, and training. In addition, the availability of more sophisticated PDC systems, such as multi-stage hybrid systems, is constrained by a lack of applied research and development on downdraft cooling. Familiarity with PDC systems could be increased and widespread misperceptions addressed if performance evaluation methods were more cost-effective and accessible.

The five common research methods used in studies of PDC are computational fluid dynamics (CFD) simulations [12,13], full-scale prototypes tested outdoors [14–16] or in a controlled environment [17,18], and reduced-scale prototypes tested outdoors [19] or in a controlled environment [20–22].

Table 1 outlines the advantages and limitations of each method based on an analysis of recent studies. CFD simulations require an extended time to learn how to properly use the tool without providing the ability to understand operational issues. Full-scale prototype testing indoors and outdoors can evaluate system operational issues but requires large space, detailed construction knowledge, and higher budgets to set up. Reduced-scale prototypes can be quickly fabricated and provide insights into operational challenges; however, when they are tested outdoors, data collection timeframes are bound by ambient conditions.

Table 1. Advantages and limitations of the different PDC performance evaluation methods.

Method	Example Studies	Advantages	Limitations
Computational Fluid Dynamics (CFD)	Kang and Strand [12] Ghoulem et al. [13]	Results are obtained rapidly with simplified digital models. Multiple iterations can be evaluated.	Steep learning curve associated with skillfully using the software. High costs associated with software licensing. Operational issues cannot be understood.
Full-Scale Prototypes (Outdoors)	Givoni [14] Pearlmutter, Erell, and Etzion [15] Calautit and Hughes [16]	Operational issues can be understood.	Data collection timeframe limited by ambient conditions. Detailed construction knowledge required. Construction costs can be prohibitive.
Full-Scale Prototypes (Controlled Environment)	Duong et al. [17] Mahon, Friedrich, and Hughes [18]	Operational issues can be understood. Data collection is independent of ambient conditions.	Access to a space with controllable environmental conditions can be a barrier. Detailed construction knowledge required. Construction costs can be prohibitive.
Reduced-Scale Prototypes (Outdoors)	Chakraborty and Fonseca [19]	Operational issues occurring at full scale can be understood. Basic construction knowledge makes it easy to quickly obtain results. Multiple iterations can be evaluated.	Data collection timeframe limited by ambient conditions.
Reduced-Scale Prototypes (Controlled Environment)	Chiesa and Grosso [20] Alaidroos and Krarti [21] Zaki, Richards, and Sharma [22]	Operational issues occurring at full scale can be understood. Basic construction knowledge makes it easy to rapidly obtain results. Multiple iterations can be evaluated.	Access to a space with controllable environmental conditions (typically a wind tunnel) can be prohibitive.

Reduced-scale prototype testing in a controlled environment addresses the limitations of the other four methods and provides for expanded research and development opportunities of PDC. This method allows for rapid quantitative testing of multiple design iterations as well as a qualitative understanding of operational issues that would occur at full scale. However, fully realizing the advantages of reduced-scale testing requires a controlled environment that is both affordable to build and capable of practically and reliably replicating environmental conditions year-round independent of ambient conditions. PDC reduced-scale prototype testing is typically conducted inside wind tunnels of various

scales [23,24] which are complex to build and commission. In addition, they require capital and space investments even greater than what is required for full-scale prototypes.

The design, construction, and commissioning of a novel environmental test chamber intended to overcome cost, space, and complexity limitations of existing facilities, as well as allow the advantages of PDC reduced-scale prototyping to be more widely realized, is described in the next section.

2. Materials and Methods

Having established the overarching design goal described above, the following design criteria were identified to meet that goal:

1. The chamber should allow for maximized prototype scale reduction, to fully leverage cost and design iteration efficiencies.
2. The chamber's operational parameters should be accurate and repeatable enough to collect usable data from reduced-scale prototypes.
3. The chamber should be capable of reproducing the temperatures, humidity levels, and air velocities recorded from PDECT full-scale prototype datasets [25], allowing chamber characterization and calibration of reduced-scale prototype data.
4. The chamber should be constructible within a relatively modest budget.
5. The chamber should be self-contained and therefore available to users without access to large indoor spaces or special facilities.

2.1. Resources

The available site and construction resources influenced the specific design of the chamber, driving additional design criteria and constraining possible design choices. The site is an outdoor concrete pad approximately 9.1 m × 18.2 m (30′-0″ × 60′-0″) previously occupied by a metal building and lacks ready access to grid electricity The budget for initial construction (labor plus a portion of the materials) was modest (USD 10,000); however, this was supplemented with in-kind donations including the following: a 6.10 m (20′-0″) standard shipping container; EPS geofoam panels 150 mm (6″) thick; 12,000 BTU mini-split heat pump; and 3480-watt photovoltaic array, along with DC-AC inverter and 2400 amp-hour battery bank.

2.2. Chamber Design

Initial design decisions sought to leverage available resources and satisfy budget and space constraints without compromising other design criteria. The shipping container was used as the exterior shell of the chamber; chamber electrical needs were supplied via the photovoltaic panels and battery bank; the mini-split heat pump was used for primary heating, cooling, and dehumidification control; and the geofoam panels were used as interior insulation to moderate heat exchange with the outer environment and boost the efficiency of chamber environmental controls. To minimize friction and turbulence, the geofoam panels were clad with 22-gauge galvanized sheet metal, selected for workability and economy. The same material was also used for corner fairings and the center divider. The use of galvanized sheet metal was designed not only to fulfill primary budgetary and operational goals, but also to minimize emissions, allowing for secondary uses of the chamber.

Based on the review of literature, it was determined that an array of multi-speed, high-volume, high-velocity fans circulating air in a closed-loop oval raceway would allow for maximal air velocity in the chamber, and thus maximize prototype scale reduction when simulating wind speeds recorded in existing full-scale datasets. The raceway was formed by fairing all four interior corners and adding an oval floor-to-ceiling divider roughly centered in the chamber as illustrated in Figure 2.

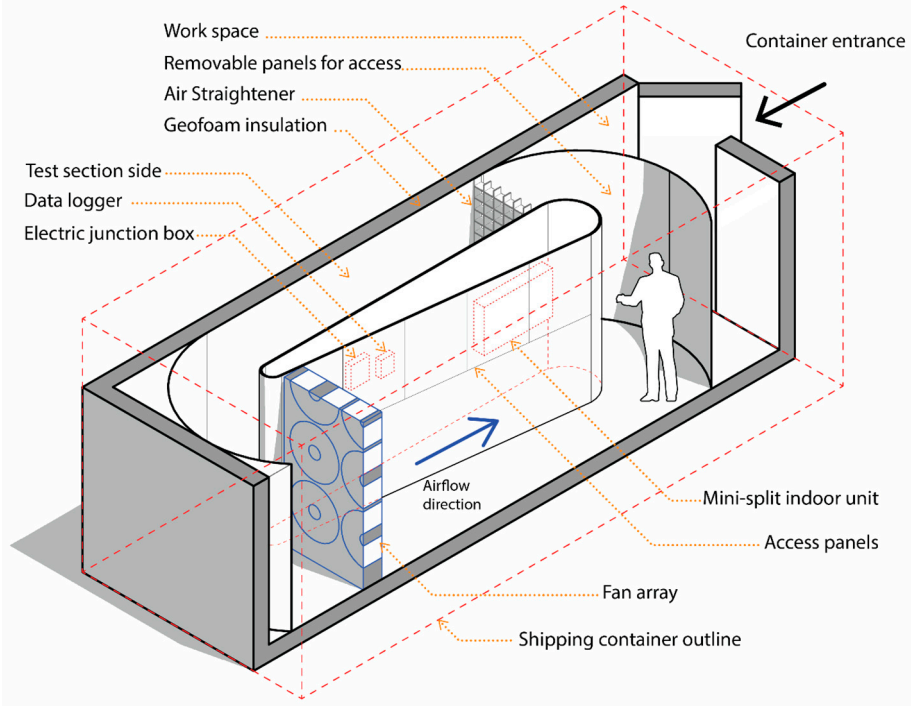

Figure 2. Three-dimensional diagram explaining test chamber overall concept.

Total power required by the chamber including sizing the maximum electrical load available for the fans (P_{fans}) required balancing available solar power generation (P_{pv}) with test run times (T_{test}), resulting in Equation (1). P_{pv} was estimated using the U.S. National Renewable Energy Laboratory online calculator (pvwatts.nrel.gov) given the chamber location, orientation, photovoltaic panel nameplate generation, and efficiency of inverter and battery storage.

$$P_{fans} = \frac{P_{pv} \times 12}{T_{test}} - \left(P_{hp} + P_{misc}\right) \quad (1)$$

Values from May, June, and July were averaged at 1.40 kW and multiplied by a conservatively estimated 12 h of available daylight. P_{hp} is the electrical load due to the heat pump (1.86 kW), and P_{misc} represents plug loads of sensors, data loggers, laptop, and other equipment for future expansion (2.40 kW). The remaining maximum loads usable for fans as well as budget and space constraints resulted in choosing an array of six fans moving air at a rate of 807 m^3/min (28,500 ft^3/min). These together draw a total of 40.17 amps (770 W @ 115 V × 6) and allow for off-grid test run times (T_{test}) of approximately two hours per day during late spring and summer with all systems operating, which was deemed adequate.

To correlate chamber results with results from full-scale prototype investigations previously conducted by Al-Hassawi, 2020, maintaining a consistent volumetric flow rate (Q) between the two studies requires an increase in flow velocity (V_{in}) as the vertical surface area of the tower inlet facing the wind (A) becomes smaller (Equation (2)).

$$Q = V_{in} \cdot A \quad (2)$$

Therefore, the effective lower boundary for scale reduction can be derived using Equation (3) where the scale factor (C) is the relationship between air velocity at the tower inlet from full-scale testing (V_{in}) and air velocity in the test side of the chamber is established through computational fluid dynamics (CFD) analysis (V_{cfd}).

$$C = \frac{V_{in}}{V_{cfd}} \quad (3)$$

The design of the chamber raceway, including fan array placement, corner fairing radii, and center divider sectional geometry, was refined through an iterative series of CFD simulations using the Autodesk CFD 2019 software. Three-dimensional modeling was developed in Autodesk Revit 2019 and focused on the geometry surrounding the air flow path. To expedite run times, a simplified orthogonal grid geometry for the air straightener at 0.1 m × 0.1 m (4″ × 4″) (H × W) was used and was placed perpendicular to the air flow path. Since the purpose of the simulations was to compare multiple options to one another, material default values in CFD software were assigned to 3D objects and were kept consistent across all schemes. Rigid Styrofoam insulation was used for the enclosure, plywood for the air straightener, a fan material customized to the manufacturer's fan curves for the fan array, and air for the interior void. Closed-loop air movement was generated through fan-initiated air flow on the supply side and a static pressure of zero on the return side to keep air cycling in the chamber. An automated mesh was generated for all iterations with an average mesh count of approximately 500,000 cells.

More than 20 variations were examined with different center divider geometries, test section dimensions, air flow directions, air straightener placement, and fan array placement to understand their impact on air velocities in the test section. Figure 3 illustrates six representative plan views taken from the series, leading to iteration F which meets construction and air flow constraints. The test section measures at 2.0 m × 0.6 m × 3.0 m (6′-10″ × 2′-0″ × 10′-0″) (H × W × D), and air flows counterclockwise looping around a 3.0 m (10′-0″) center divider with a tapered horizontal cross section and faired ends with radii of 260 mm (10 1/2″) and 100 mm (4″). The taper restricts air flow so that air velocity increases as it enters the test section. The air flow path then widens as it exits the test section and declines in velocity prior to returning through the fans and beginning a new cycle.

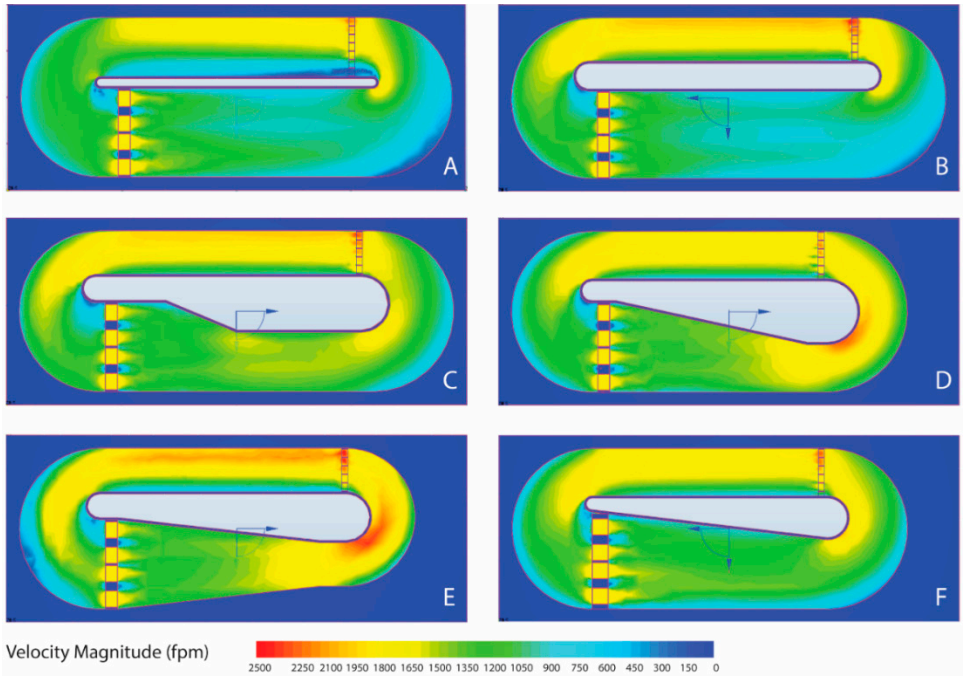

Figure 3. Floor plan views from CFD simulation results with option F being the preferred iteration. (**A**) narrow center divider with no taper. (**B**) wide center divider with no taper. (**C**) wide center divider angled on the fan-side. (**D**) acute taper in the center divider on the fan-side. (**E**) shallow taper in the two walls on the fan-side. (**F**) shallow taper in the center divider on the fan-side.

Measured outdoor air velocities during full-scale prototype investigations averaged 2.25 m/s (444 fpm). CFD simulations give a maximum fan-side velocity of 6.86 m/s (1350 fpm) and test-side velocity of 9.17 m/s (1805 fpm). Therefore, the calculated scale factor using Equation (3) is 0.24, or a 1:4 ratio. Actual air velocity in the test chamber is assumed to be lower than predicted velocities, due to sources of turbulence and friction not necessarily captured by the CFD simulation; thus, a conservative ratio of 1:3 is assumed for reduced-scale models.

2.3. Chamber Construction Details

Construction of the chamber took place between January and October 2021. The shipping container's long axis was directed northwest to southeast, which is the optimum solar orientation given pad dimensions and site conditions.

North–south and east–west perspective sections (Figures 4 and 5, respectively) highlight key components of the chamber, including an auxiliary "doghouse" shed with dimensions of approximately 1.8 m × 2.4 m × 2.4 m (6′-0″ × 8′-0″ × 8-0″) (H × W × D). This room houses the battery bank and inverter and provides a mounting surface on the roof for 3 of the 12 photovoltaic panels.

The shipping container is insulated on five of six interior sides with 150 mm (6″) reclaimed EPS geofoam panels (total R-24 or greater). Container doors are insulated with 100 mm (4″) Type 1 EPS rigid foam (total R-16). Foam insulation and 22-gauge galvanized sheet metal panels are attached using polyurethane construction adhesive, with seams between panels lapped and staggered. Joints are sealed with aluminum HVAC tape to reduce friction. Galvanized ceiling panels are attached to 50 mm × 50 mm (2″ × 2″) nominal wood furring, creating a chase for electrical and data cables. Corner fairings are 22-gauge galvanized sheet metal panels, mounted with screws to light gauge steel stud and 19 mm (3/4″) nominal plywood frames. Fairings on the door side of the container are removable, whereas fairings on the opposite side are fixed.

The center divider is made with tubular cardboard concrete forms used to shape the end radii. Access panels are cut into the cladding sheets, allowing the mini-split indoor unit, the data logger, and the electrical service panel to be mounted in the divider interior. The access panel over the mini-split unit is perforated, allowing air to flow into the fan side of the chamber.

The fan array is constructed from 41 mm (1–5/8″) slotted strut channel and channel connectors, bolted to the fan flanges. The frame is friction fit between the chamber floor and ceiling and further secured with 90-degree steel angles and screws. A 12.7 mm × 12.7 mm (1/2″ × 1/2″) galvanized steel mesh was placed on the return side of the frame to protect the fan blades from any large-scale objects that could potentially detach from the prototype models. The air straightener grid has clear perforation dimensions of 25.4 mm × 25.4 mm × 76.2 mm (1″ × 1″ × 3″) (H × W × D) and is made from 3.2 mm (1/8″) MDF panels cut down to stripes using a flatbed laser cutter. Pieces are notched into each other and held in place with friction.

Three weather-proof ports are constructed from 50 mm (2″) nominal ABS DWV pipe, passing through holes cut through chamber walls and insulation, sealed in place with spray foam and flashed with roof vent boots. These were used for passage of electrical and data conduits, mini-split coolant lines, and a water supply hose connecting between the misters and the 23 L (6 gallons) 40 psi portable pressurized water tank.

Photovoltaic panels on the roof of the shipping container are ganged together in groups of three using a proprietary aluminum channel system and then attached to a frame angled at 45 degrees constructed using a 25 mm (1–5/8″) slotted strut channel and connectors. Doghouse photovoltaic panels are attached directly to the roof using the proprietary aluminum channel system. The doghouse battery and inverter shed uses conventional 50 mm × 100 mm (2″ × 4″) nominal wood construction, clad with corrugated siding and roofing. Figure 6 consists of a series of photos from the chamber construction, and Figure 7 is an overall photo of the completed test chamber.

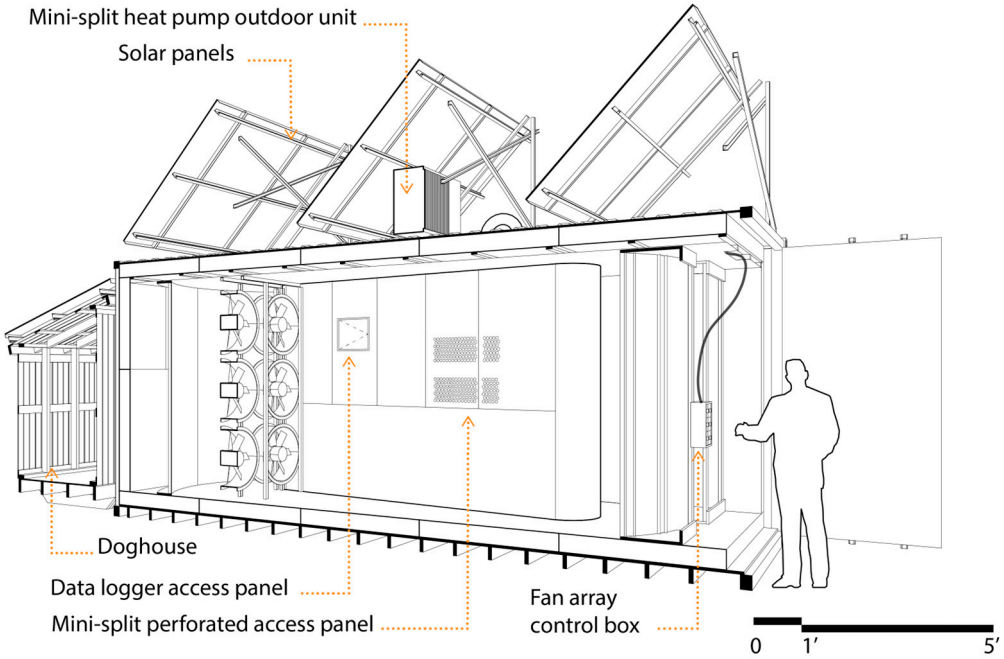

Figure 4. North–south perspective section through test chamber and doghouse.

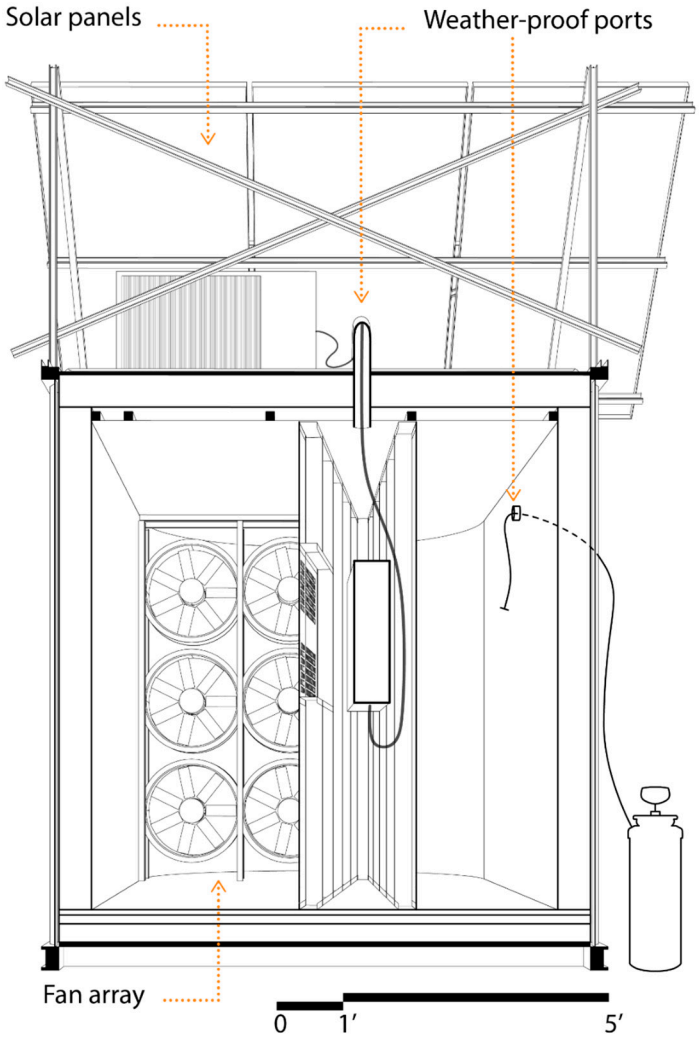

Figure 5. East–west perspective section through test chamber.

Figure 6. Test chamber construction photos. (**1**) Battery rack in doghouse. (**2**) Perforated access panel for mini-split indoor unit. (**3**) Air straightener placed in chamber test side. (**4**) Fan array fixed in place. (**5**) Weather-proof port connecting doghouse to chamber. (**6**) Door-side corner fairings.

Figure 7. Overall photo of the completed test chamber from northwest corner.

2.4. Chamber Data Collection Equipment

Like the full-scale investigations by Al-Hassawi, a customized system completely supplied by Onset Computer Corporation was assembled to measure and record conditions inside the test section. Due to the extreme environmental conditions predicted inside the chamber, the RX3002-00-01 Data Logger was selected because of its weatherproof enclosure rated for outdoor use. The logger has a time accuracy of ±8 s per month in a 0° to 40 °C (32 °F to 104 °F) range. One RXMOD-A1 4-channel Analog Module was installed, and the following sensors were attached to the logger:

- Two S-THB-M008 temperature/relative humidity smart sensors with a temperature accuracy of ±0.21 °C (0.38 °F) from 0° to 50 °C (32–122 °F) and RH accuracy of ±2.5% from 10% to 90% attached to the logger's smart sensor ports.
- Two T-DCI-F300-1C3 air velocity analog sensors which can read velocities that range between 1.0 and 20 m/s (200 and 4000 fpm) with an accuracy of ±5% of reading at +0.15 m/s (+30 fpm) attached to the logger's analog module.

Logging intervals were identical to the full-scale experiment and set to 30 s followed by averaging every ten recordings to obtain measurements at five-minute intervals. One temp/RH sensor and one air velocity sensor were located at the tower inlet which is 1.5 m (5′-0″) above the interior finish level on the air-entering side of the test section. The other two sensors were located at the tower outlet 0.3 m (1′-0″) above the interior finish level on the side where air is exiting the test section. The outlet sensors were placed inside a box open from the front and back and made from polyisocyanurate insulation to accurately capture the air variables at the tower outlet and isolate the sensors from the hotter chamber conditions.

2.5. Chamber Commissioning

Chamber commissioning included a characterization phase, to determine specific operational characteristics of the chamber, and a calibration phase, to correlate results from testing a reduced-scale prototype in the chamber with prior datasets from testing a full-scale downdraft evaporative cooling prototype under ambient conditions.

2.5.1. Chamber Characterization and Determination of Operational Modes

All chamber systems were operated at first to ensure that the data collection equipment, the fan array, and the mini-split heat pump properly function off-grid for the durations anticipated during testing. The chamber was then characterized in a two-step process followed by collecting data from the reduced-scale prototype as follows:

1. Characterization of air velocities obtained from the fan array was accomplished using three operational modes. Performance in each mode was characterized under a range of fan array conditions, varying both the speed of fans in the array (low, medium, high) and the total array capacity (one-third, two-thirds, full). Test runs at each speed lasted a minimum of 60 min, during which array capacity was increased by incrementally powering up fan pairs from top to bottom. The tested modes are as follows:

   A: Fans on, test section empty, no air straightener.
   B: Fans on, test section empty, air straightener in place.
   C: Fans on, prototype in test section, no air straightener.

2. Characterization of temperature and relative humidity levels obtained from the heating system was accomplished using two operational modes. Temperatures were brought up to a target point and were maintained at a steady state for at least 30 min, replicating how the chamber would be set up prior to running the misters in the prototype. The tested modes are as follows:

   D: Fans on, auxiliary heat on, test section empty.
   E: Fans on, auxiliary heat on, prototype in test section.

3. Downdraft evaporative cooling prototype calibration utilized two operational modes. Each mode was repeated at least five times; each time, one mister ran on a duty cycle of 30–60 min, resulting in over 225 min of total run time. Water temperatures supplied to the mister averaged 12.5 °C (55 °F), similar to water supply temperatures recorded during full-scale testing. The tested modes are as follows:

F: Fans on, auxiliary heat on.
G: Fans off, auxiliary heat on.

2.5.2. Chamber Calibration

To calibrate results from the chamber with data collected from testing the downdraft evaporative cooling full-scale prototype, a 1:3 reduced-scale model was built. The full-scale tower had shaft dimensions of 3.0 m × 0.9 m × 0.9 m (10′-0″ × 2′-8″ × 2-8″) (H × W × D), whereas the reduced-scale model shaft dimensions were 1.1 m × 0.3 m × 0.3 m (3′-9″ × 1′-0″ × 1-0″). Both prototypes used misting nozzles with a maximum allowable pressure of 160 psi. Both prototypes had the capability of incorporating three misting nozzles, each with a water flow rate of 2.6 L/h (0.7 gal/h) for a total water supply of 8.0 L/h (2.1 gal/h). Preliminary testing was conducted with one nozzle installed, and the materials used to build the tower enclosure were identical to those used in the full-scale experiment. The structure was made of metal angles, the enclosure from 20 mm (3/4″) polyisocyanurate insulation, and the inlet from 6 mm (1/4″) nominal plywood. Figure 8 is a north–south perspective section through the test side describing the prototype's location in relation to the two sets of sensors.

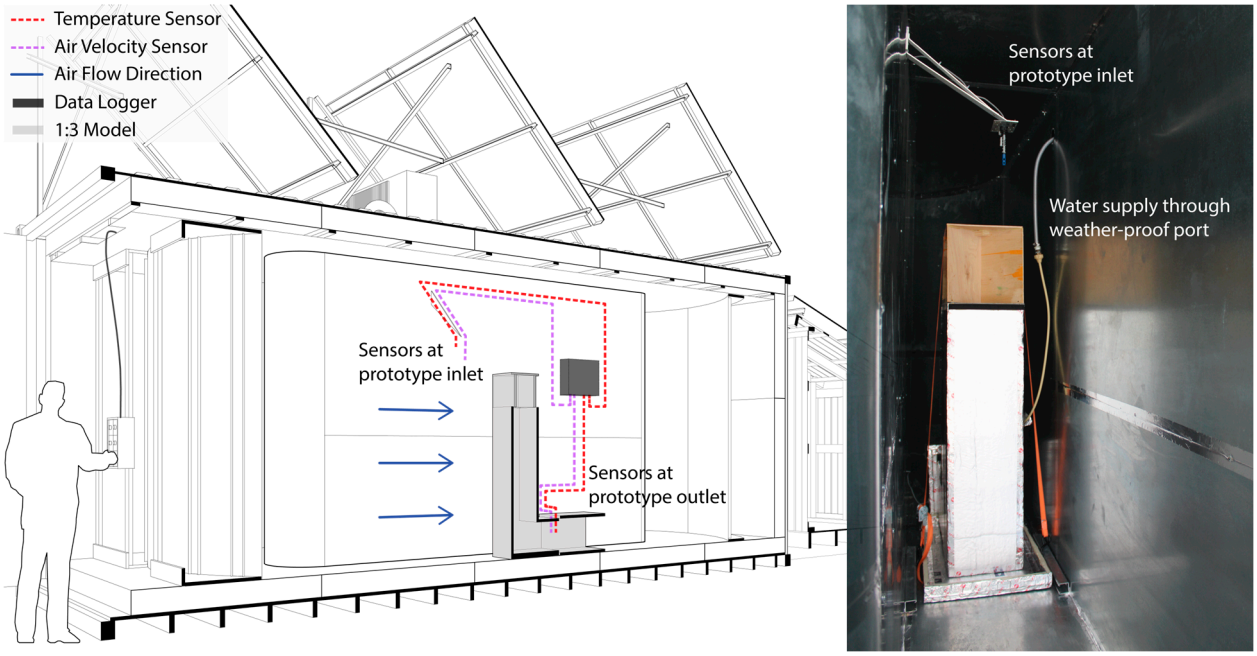

Figure 8. North–south perspective section indicating sensors and reduced-scale prototype locations in the test side of the chamber (**left**). Image of prototype placed inside the chamber (**right**).

Tables 2 and 3 outline data collected from the full-scale investigation over four days or 1620 min of operation equating to 317 data collection samples. Table 2 lists the ambient conditions at the tower inlet, whereas Table 3 lists conditions at the tower outlet. Overall, average ambient conditions were 43 °C (109 °F) dry-bulb temperature, 7% RH, and 2.25 m/s (444 fpm) wind speed. Additionally, average conditions at the tower outlet from one mister operating were 12 °C (22 °F) drop in temperature (ΔT), 15% increase in relative humidity (ΔRH), and 0.92 m/s (182 fpm) air velocity (V_{out}).

Table 2. Average ambient conditions collected at tower inlet during full-scale investigation: dry-bulb temperature ($T_{DB\text{-}in}$), relative humidity (RH_{in}), and wind speed (V_{in}).

Date	$T_{DB\text{-}in}$-°C (°F)	RH-%	V_{in}-m/s (fpm)
14 June 2017	39 (103)	4	1.75 (346)
15 June 2017	42 (107)	5	1.57 (311)
18 June 2017	43 (110)	9	2.31 (455)
21 June 2017	46 (115)	10	3.36 (662)
Average	43 (109)	7	2.25 (444)

Table 3. Average conditions at downdraft evaporative cooling tower outlet collected during full-scale investigation: temperature drop (ΔT), relative humidity rise (ΔRH), and air velocity (V_{out}).

Date	ΔT-°C (°F)	ΔRH-%	V_{out}-m/s (fpm)
14 June 2017	12 (23)	15	0.82 (162)
15 June 2017	17 (32)	25	0.82 (162)
18 June 2017	11 (21)	13	0.93 (184)
21 June 2017	9 (16)	7	1.12 (221)
Average	12 (22)	15	0.92 (182)

3. Results and Discussion

3.1. Chamber Commissioning

All chamber systems function as designed, with some limitations:

- Using the heat pump as the primary heat source stabilized temperatures at a maximum of 31 °C (88 °F) which was the maximum temperature the heat pump could achieve before shutting off. An auxiliary heat source was deemed necessary to reach and maintain higher temperatures in the chamber.
- Operation in below-freezing conditions requires more preheating time for the chamber to reach test temperatures, with energy demand for preheating exceeding battery storage when the mini-split heat pump is used. The use of auxiliary space heaters, either electrical resistance or propane-fired connected to grid electricity, allows for rapid heating of the chamber, although the latter is not ideal from an indoor air quality perspective.
- Battery capacity and recharge times limit test durations during winter months to a maximum of two hours per day. This contrasts with summer tests which allow for morning and afternoon runs for a total daily test duration of up to six hours.
- Chamber insulation is sufficient to retain most of the waste heat from fan operation and air friction, and this interferes with the establishment of steady-state conditions. During preliminary characterization test runs, rising temperatures inside the chamber reached as high as 60 °C (140 °F). Subsequent testing showed that chamber venting is required to maintain temperatures at a steady state. Currently, venting is accomplished by opening one of the insulated chamber doors and shifting door-side corner fairings to create a small gap of 50 mm (2″).
- Low relative humidity levels (below 10%) observed during full-scale prototype testing proved challenging to achieve, especially with misters running. Within the chamber, RH levels at the tower inlet averaged 15% and continued to increase slightly when misters were operating.

3.2. Characterization of Air Velocities

With the test section empty and no air straightener (operational mode A), average peak air velocities exceeded CFD predictions, reaching 11.87 m/s (2337 fpm) (Figure 9). In principle, this allows a scale reduction factor of 1:5 or greater; however, chamber operation with a prototype in place significantly reduces air velocity. Sensor readings revealed an air velocity differential (ΔV_{air}) between the top and bottom of the chamber's test section. This

was true for all speeds and array capacities. ΔV_{air} decreased as array capacity increased, ranging from 3.15 m/s (620 fpm) with two fans to 0.30 m/s (60 fpm) with six fans. Contrary to expectations, the lower sensor (air velocity at outlet) recorded higher velocities than the upper sensor (air velocity at inlet) when the upper pair of fans were operating. This can be attributed to the positioning of the lower sensor inside a protective box open along the path of air flow, creating a Venturi effect and increasing velocity.

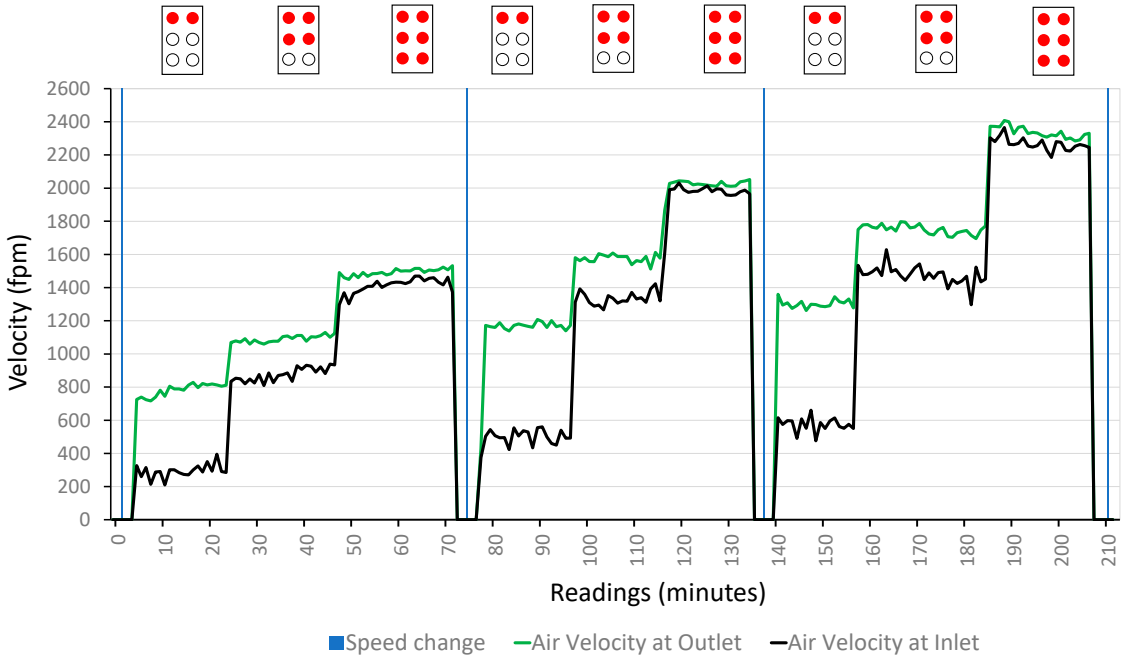

Figure 9. Air velocities, operational mode A: chamber empty.

With the air straightener device in place (operational mode B), measured air velocities in the test section nearly aligned with CFD predictions, reaching an average of 9.06 m/s (1785 fpm) (Figure 10). There was a significant decrease in the air velocity differential (ΔV_{air}) between top and bottom sensor readings, ranging from 1.52 m/s (300 fpm) with two fans running to 0.06 m/s (12 fpm) with all fans running. Adding the air straightener resulted in the upper sensor recording speeds higher than the lower sensor, and the differential between the two sensors declined steeply with four or six fans operating, thus better aligning with initial expectations.

Adding the downdraft cooling prototype to the test section with no air straightener (operational mode C) resulted in greater air velocity differentials between upper and lower sensors from those observed in previously evaluated operational modes. At all speeds, with two or four fans operating, velocities at the prototype outlet fell below the lower sensitivity limit of the air velocity sensor 1.00 m/s (200 fpm). Velocities at the outlet averaged 2.33 m/s (459 fpm), 1.83 m/s (362 fpm), and 1.17 m/s (231 fpm) when all fans were running at high, medium, and low speeds, respectively (Figure 11). Average inlet velocities of 8.55 m/s (1684 fpm) were observed with all fans running at high speed, and average inlet velocities of 7.90 m/s (1554 fpm) were observed with all fans running at medium speed. These values exceed the target air velocity of 6.76 m/s (1332 fpm), required to match scale-corrected velocities from the full-scale investigation datasets. Volumetric flow rates at tower inlet vertical surface area calculated for one of the four sides perpendicular to airflow averaged 63 m^3/min (2235 cfm) from the reduced-scale prototype with fans running at medium speed, versus 65 m^3/min (2415 cfm) from full-scale investigations. This close alignment between the scales can be further refined by modifying air speeds.

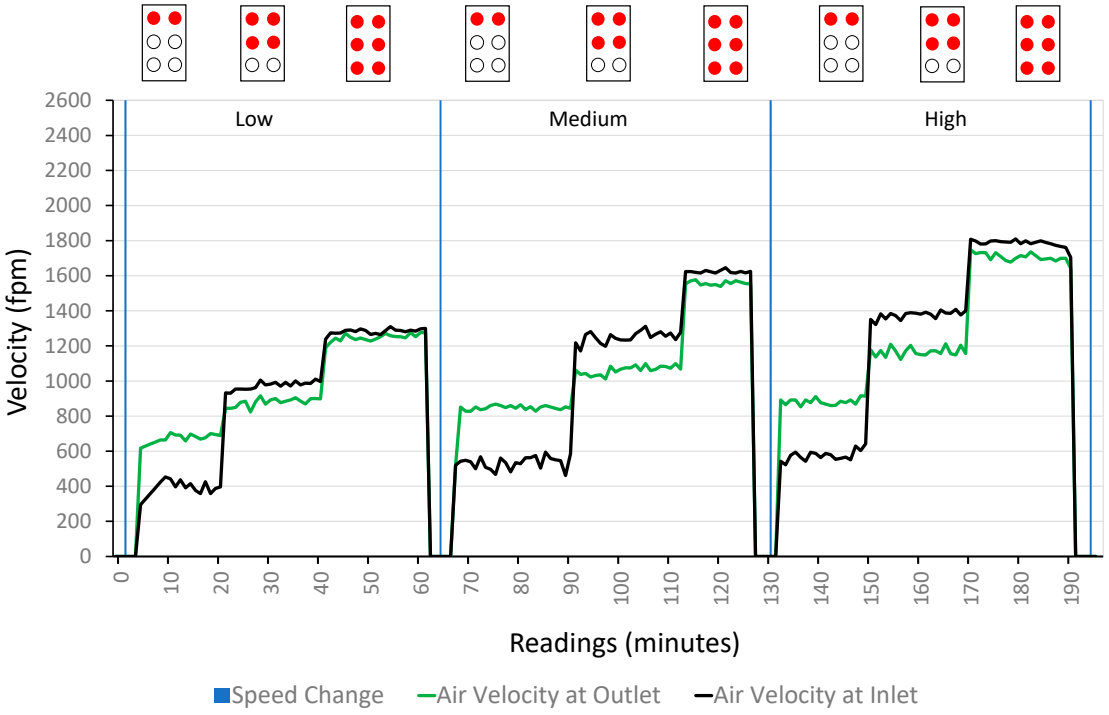

Figure 10. Air velocities, operational mode B: air straightener in place.

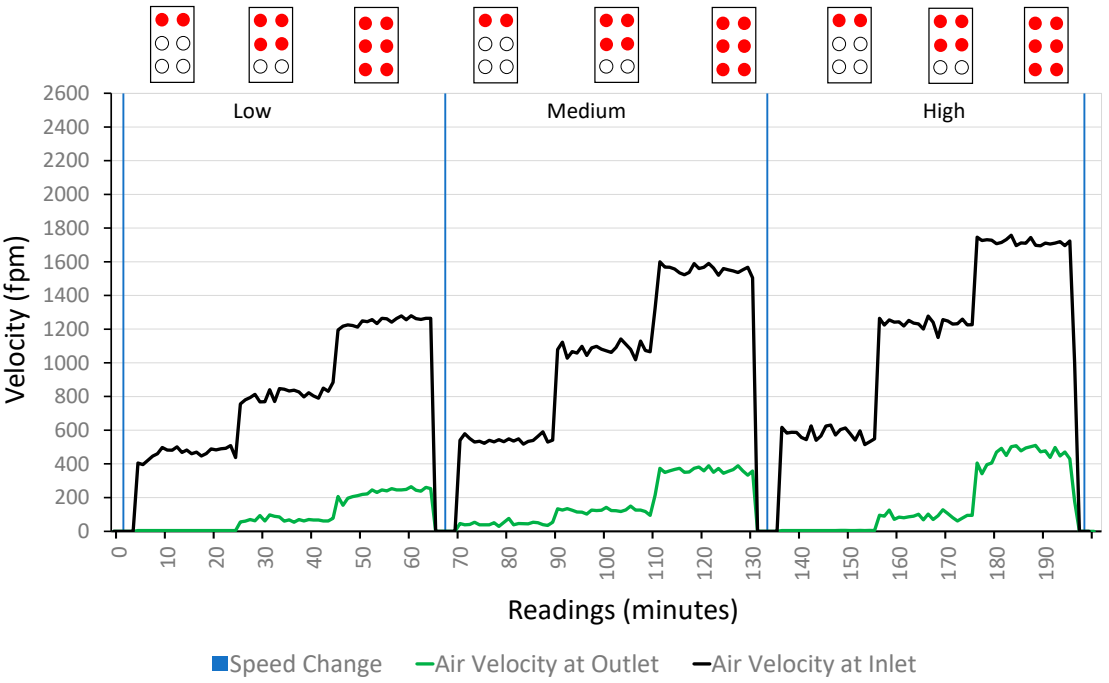

Figure 11. Air velocities, operational mode C: prototype in test section (no air straightener).

As a result of air velocity characterization, it was determined the most accurate and energy-efficient data collection mode would occur with the fan array operating at full capacity (six fans), and fan speeds set between low and medium to meet the target air velocity. Furthermore, it was determined that prototype evaluation should occur without the air straightener device in place, as the presence of the device further reduced air velocities in the chamber.

3.3. Characterization of Temperature and Relative Humidity Levels

With the test section empty (operational mode D), a maximum steady-state temperature of 49 °C (120 °F) at 10% coincident relative humidity can be maintained using auxiliary heat and the venting technique described above. Upon the addition of the tower in the test side with no misters running (operational mode E), the two sets of sensors continued to produce consistent recordings, with temperatures remaining within ±0.5 °C (±1 °F) of each other and RH levels varying by ±2.5%.

3.4. Downdraft Evaporative Cooling Prototype Calibration in the Chamber

In operational mode F, running the mister with the fan and auxiliary heat on proved challenging in maintaining a steady-state temperature and relative humidity levels at the tower inlet. Throughout one test run, inlet temperatures continued to decline by approximately (2 °C (4 °F)), and inlet relative humidity levels increased by 6%. Temperature drops between inlet and outlet were approximately half of what was observed at full scale. This can be attributed to the short contact time between the hot air and the water in the tower shaft due to the shorter tower shaft height resulting in quicker downward air movement caused by fan operation. On the other hand, RH increase and tower outlet velocities were slightly higher than observations made at full scale.

Figure 12 graphs data from this mode of prototype evaluation where chamber conditions at the beginning of mister operation were set to 41 °C (107 °F), 16% RH, and 6.76 m/s (1332 fpm) air velocity. Operating the mister for 40 min resulted in average tower outlet conditions of 34 °C (93 °F) in temperature or a drop of 6 °C (10 °F), 33% in RH or a rise of 13%, and 1.31 m/s (259 fpm) in air velocity. These differences between inlet and outlet conditions remained relatively consistent throughout multiple test runs despite slight changes in tower inlet conditions.

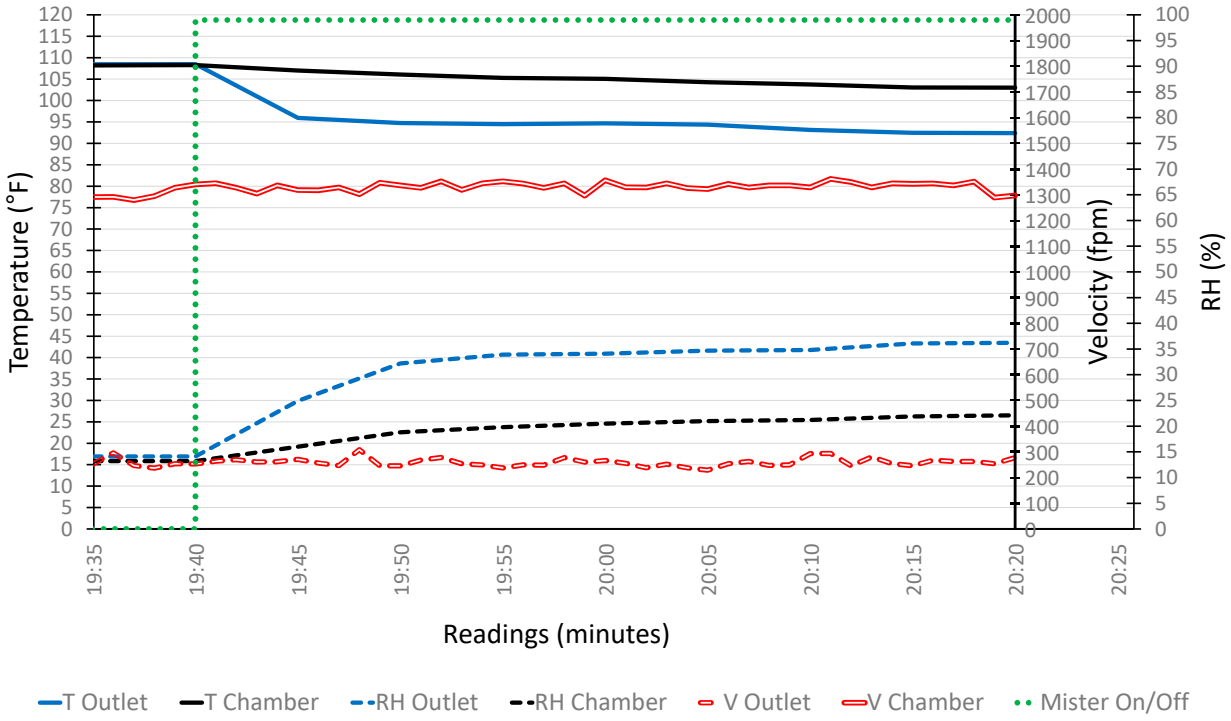

Figure 12. Data from operational mode F: one mister on, auxiliary heat on, and fans on.

In operational mode G, running the mister with the fan off and auxiliary heat on resulted in a decline in outlet temperatures while maintaining the chamber's overall temperature throughout one test run within ±1 °C (2 °F) of steady-state conditions. However, relative humidity levels increased by 12% due to the lack of a drain for the unevaporated mister water directly to the outside of the chamber. Figure 13 graphs data from this mode

of prototype evaluation where chamber conditions at the beginning of mister operation were set to a temperature of 40 °C (104 °F) and RH level of 16%. Operating the mister for 75 min resulted in average tower outlet conditions of 29 °C (85 °F) in temperature (a drop of 11 °C (19 °F)) and 53% in RH (a rise of 29%). These differences between inlet and outlet conditions remained relatively consistent throughout multiple test runs.

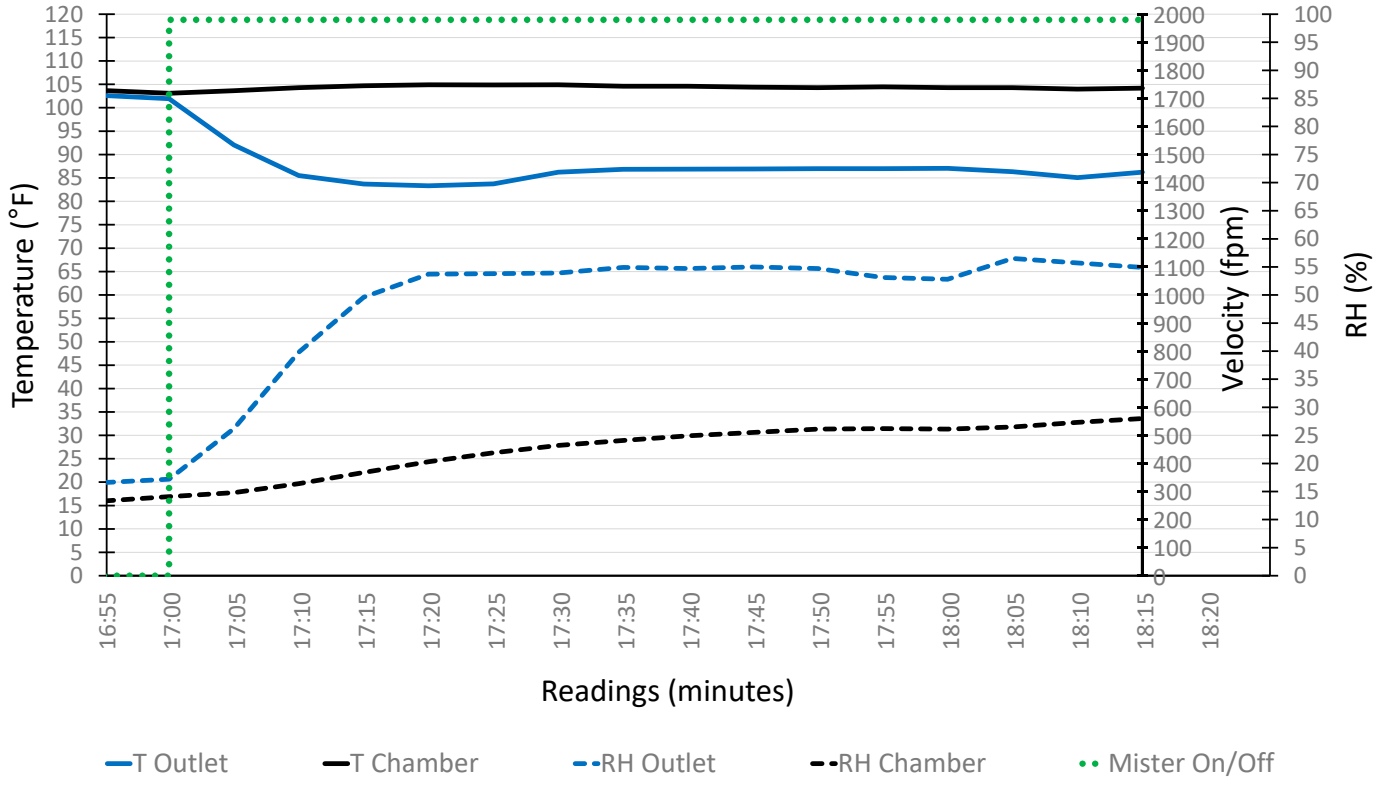

Figure 13. Data from operational mode G: one mister on, auxiliary heat on, and fans off.

The system's actual cooling relative to the theoretical maximum that could be produced was estimated by calculating the evaporative efficiency. This variable was preferred for further statistical analysis as opposed to analyzing temperature and humidity independently because it allows for comparing the system's combined effect on temperature drop and humidity rise at different scales even though tower inlet conditions do not exactly match. Evaporative efficiencies (ϵ_{evap}) were calculated using Equation (4) below where (T_{DBin}) is the entering air dry-bulb temperature, (T_{WBin}) is the entering air wet-bulb temperature, and (T_{DBout}) is the exiting air dry-bulb temperature.

$$\epsilon_{evap} = \frac{T_{DB-in} - T_{DB-out}}{T_{DB-in} - T_{WB-in}} \quad (4)$$

Operational mode G was selected for comparing evaporative efficiencies between full- and reduced-scale experiments because it resulted in similar temperature drops. A subset of the data from full-scale experimentation was selected which had one mister operating and ambient air dry-bulb temperatures nearly identical to temperatures witnessed in the chamber at the tower inlet or a range between 39 °C and 40 °C (103 °F and 105 °F). Twenty-two data samples from the full-scale experiment resulted in average evaporative efficiencies of 62% and a standard deviation of 6.4%, whereas 15 data samples from operational mode G produced average evaporative efficiencies of 63% and a standard deviation of 3.8%. The absolute uncertainty of the evaporative efficiency calculated from the chamber prototype data was ±1% (0.015 relative uncertainty) compared to an absolute uncertainty of ±2% (0.032 relative uncertainty) from the full-scale prototype.

An independent sample two-tailed t-test with a confidence interval of 95 percent indicated no significant difference between evaporative efficiencies calculated at the two scales with a *p*-value of 0.75 and a Cohen's d lower limit of −0.76 and upper limit of 0.55. The effect size difference between the group means of 0.11 shows that a very small to small difference existed, in accordance with Sawilowsky (2009) [26], with the reduced-scale prototype having slightly higher evaporative efficiency. However, the confidence interval suggests that either setting may have higher, lower, or equal evaporative efficiency in the population.

Operational mode F was selected for comparing outlet air velocities between full- and reduced-scale experiments because it had the fans operating and met the target inlet air velocity. A subset of the data from full-scale experimentation was selected which had one mister operating and ambient wind speeds nearly identical to speeds witnessed in the chamber at the tower inlet or a range between 2.13 m/s and 2.33 m/s (420 fpm and 460 fpm). Twenty-two data samples from the full-scale experiment resulted in average velocities at tower outlet of 0.86 m/s (170 fpm) and a standard deviation of 0.09 m/s (19 fpm), whereas 35 data samples from operational mode F produced average velocities at tower outlet of 1.31 m/s (259 fpm) and an identical standard deviation of 0.09 m/s (19 fpm).

An independent sample two-tailed t-test with a confidence interval of 95 percent indicated that there is a difference between the velocities recorded from the two scales with a *p*-value < 0.05. This was enforced by the high effect size difference of 4.7 between the group means, with the reduced-scale prototype having higher velocities. This difference can be attributed to the air flowing down the tower shaft from one direction in the chamber unlike actual conditions where air is entering the tower from multiple directions and wind speeds are constantly changing.

Table 4 describes average conditions for temperature drops (ΔT), relative humidity rise (ΔRH), and outlet air velocity (V_{out}) obtained from data used in statistical analysis at the two scales. The root mean square error (RMSE), the mean absolute percentage error (MAPE), and the coefficient of variation of the root mean square error (CVRMSE) were calculated for the three measured variables. Equation (5) represents CVRMSE where Y_{rs} represents data collected from the chamber and Y_{fs} represents data from full-scale experimentation.

$$CVRMSE = \frac{1}{\overline{Y_{rs}}}\sqrt{\frac{1}{n}\sum_{i=1}^{n}\left(Y_{rs,i} - Y_{fs,i}\right)^2} \quad (5)$$

The proximity of outlet air velocity was calculated using data collected under operation mode F and provided a CVRMSE of 34.4%. The proximity of temperature drops and relative humidity rise were calculated using data collected under operation mode G and provided a CVRMSE of 45.5% and 34.4%, respectively. Using the average conditions from the entire dataset collected at full scale (Table 3) resulted in stronger alignment between the two scales in V_{out} and ΔT with a CVRMSE of 29.9% and 19.6%, respectively. However, ΔRH had a higher CVRMSE of 49.9%.

Table 4. Chamber data validation of average temperature drop (ΔT), relative humidity rise (ΔRH), and outlet air velocity (V_{out}) using a subset of data from full-scale operation.

	Full-Scale Avg.	Reduced-Scale Avg.	RMSE	MAPE (%)	CVRMSE (%)
V_{out}-m/s (fpm) [1]	0.86 (170)	1.31 (259)	0.45 (89.0)	52	34.4
ΔT-°C (°F) [2]	14 (27)	11 (19)	4.70 (8.47)	31	45.5
ΔRH-% [2]	19.30	29.00	9.96	50	34.4

[1] Operational mode F. [2] Operational mode G.

4. Conclusions

Chamber construction was completed with minimal initial design modifications, and project design criteria were met with a total project budget including student labor of

USD 19,000. CFD simulation proved effective as a design tool and will be valuable for redesigning the chamber interior if different performance characteristics are desired.

Shortcomings from preliminary data collection of the prototype operating inside the chamber indicated the limitation of collecting air velocity data simultaneously with temperature/RH data. Initial recommendations are to understand outlet air velocities with fans and auxiliary heat on (operational mode F) and to understand outlet temperature and RH levels and evaporative efficiencies with fans off and auxiliary heat on (operational mode G). Fans are used in operational mode G only to mix the air inside the chamber prior to turning on the misters.

No significant difference between evaporative efficiencies calculated at the two scales was reported. An independent sample two-tailed t-test with a confidence interval of 95 percent returned a p-value of 0.755 and a Cohen's d value lower limit of -0.76 and upper limit of 0.55. Higher air velocities at the tower outlet were consistently reported in the reduced-scale model with an RMSE of 0.45 m/s (89 fpm) on average when inlet conditions were set to the target velocity of 6.76 m/s (1332 fpm). Outlet conditions were deemed sufficient for understanding airflow behavior through the downdraft cooling tower despite this large difference, since wind speeds and directions were constantly and rapidly changing at full scale.

Operational shortcomings of the chamber as initially constructed have been identified during commissioning. These are limited test duration times during below-freezing conditions due to increased battery recharge times, and the need for a venting system to maintain chamber temperatures and RH levels at steady state.

Three modifications are planned for the near future to address operational and data collection shortcomings. The first is adding a thermostatically controlled vent fan to the system which is expected to help lower and stabilize RH levels. This, coupled with the second modification of adding a drain that directs the excess unevaporated misting water from the base of the prototype immediately to the outside of the chamber, is projected to correct the misalignment in data between reduced-scale and full-scale prototypes as well as prevent the increase in the chamber's RH levels during a test. The third modification is adding an option for connecting to grid power supply to allow for auxiliary battery recharging from an exterior electrical receptacle on a nearby building, thus extending winter test run times.

While there is room for incremental improvement in the design, the chamber is both novel and impactful, filling a gap in affordable test equipment for year-round testing independent of variations in outdoor climate conditions. The chamber meets the goals of maximized prototype scale reduction, repeatable and replicable climate conditions, and year-round off-grid operation.

Future studies in the chamber will involve the development of passive cooling in general and specifically passive downdraft cooling through rapid prototyping and design iteration of innovative multi-stage downdraft cooling systems maximizing the potential of reduced-scale investigation.

Author Contributions: Conceptualization, O.D.A.-H. and D.D.; Methodology, O.D.A.-H. and D.D.; Software, O.D.A.-H.; Validation, O.D.A.-H.; Formal Analysis, O.D.A.-H. and D.D.; Investigation, O.D.A.-H. and D.D.; Resources, O.D.A.-H. and D.D.; Data Curation, O.D.A.-H.; Writing—Original Draft, O.D.A.-H. and D.D.; Writing—Review and Editing, O.D.A.-H. and D.D.; Visualization, O.D.A.-H.; Supervision, O.D.A.-H. and D.D.; Project Administration, O.D.A.-H. and D.D.; Funding Acquisition, O.D.A.-H. and D.D. All authors have read and agreed to the published version of the manuscript.

Funding: This research was funded in part through a Lemelson Foundation VentureWell Faculty Grant (grant number 21142-20) and through a Washington State University School of Design and Construction Faculty Internal Seed Grant.

Data Availability Statement: The data presented in this study are available on request from the corresponding author.

Acknowledgments: We wish to acknowledge the generous support of the WSU School of Design and Construction which contributed in-kind donations of materials and equipment. In addition, we wish to acknowledge the invaluable input and support of WSU School of Design and Construction former Director Ryan Smith; of WSU Voiland College of Engineering and Architecture faculty members Tom Jobson and David Thiessen; of Voiland College staff members Miles Pepper and Scott Hansen; of the Center for Interdisciplinary Statistical Education Assistant Director Trey DeJong; and of past graduate students including Colter Nubson, Nathan Albrecht, Feras Alsodais, and Anguel Atanassov.

Conflicts of Interest: The authors declare no conflict of interest.

Nomenclature

Pfans	Electric load available for fan array (kW)
Ppv	Available solar power (kW)
Php	Electric load for heat pump (kW)
Pmisc	Electric load for miscellaneous equipment (kW)
Ttest	Test run times (minutes)
Q	Volumetric flow rate (m^3/h (cfm))
Vin	Air velocity at tower inlet measured during full-scale testing (m/s (fpm))
A	Vertical surface area of tower inlet facing wind (m^2 (ft^2))
C	Scale reduction factor
Vcfd	Air velocity on chamber test side in CFD simulations (m/s (fpm))
ϵ_{evap}	Evaporative efficiency (%)
TDBin	Dry-bulb temperature at tower inlet (°C (°F))
TDBout	Dry-bulb temperature at tower outlet (°C (°F))
TWBin	Wet-bulb temperature at tower inlet (°C (°F))
RHin	Relative humidity level at tower inlet (%)
Vout	Air velocity at tower outlet measured during full-scale testing (m/s (fpm))
ΔT	Temperature drop between tower inlet and outlet (°C (°F))
ΔRH	Relative humidity rise between tower inlet and outlet (%)
$\Delta Vair$	Velocity differential between the top and bottom of the chamber (m/s (fpm))
Yrs	Data from reduced-scale experimentation
Yfs	Data from full-scale experimentation

Abbreviations

PDECT	Passive Downdraft Evaporative Cooling Tower
PDC	Passive Downdraft Cooling
RMSE	Root Mean Square Error
MAPE	Mean Absolute Percentage Error
CVRMSE	Coefficient of Variation of Root Mean Square Error

References

1. IEA. The Future of Cooling: Opportunities for Energy-Efficient Air Conditioning. Available online: https://www.iea.org/reports/the-future-of-cooling (accessed on 3 March 2023).
2. Architecture 2030. Why the Built Environment? Available online: https://architecture2030.org/why-the-building-sector/ (accessed on 3 March 2023).
3. Santamouris, M.; Kolokotsa, D. Passive Cooling Dissipation Techniques for Buildings and Other Structures: The State of the Art. *Energy Build.* **2013**, *57*, 74–94. [CrossRef]
4. Song, Y.; Darani, K.S.; Khdair, A.I.; Abu-Rumman, G.; Kalbasi, R. A review on conventional passive cooling methods applicable to arid and warm climates considering economic cost and efficiency analysis in resource-based cities. *Energy Rep.* **2021**, *7*, 2784–2820. [CrossRef]
5. Cook, J. *Passive Cooling. Solar Heat Technologies*, 1st ed.; MIT Press: Cambridge, MA, USA, 1989.
6. Bahadori, M.N.; Dehghani-Sanij, A.; Sayigh, A. *Wind Towers: Architecture, Climate, and Sustainability*, 1st ed.; Springer International Publishing: Cham, Switzerland, 2014.
7. Cunningham, W.A.; Thompson, T.L. Passive Cooling with Natural Draft Cooling Towers in Combination with Solar Chimneys. In Proceedings of the 6th International Conference on Passive and Low Energy Architecture, Pécs, Hungary, 1–4 September 1986.
8. Ford, B.; Schiano-Phan, R.; Vallejo, J. *The Architecture of Natural Cooling*, 2nd ed.; Routledge: New York, NY, USA, 2020.
9. Ford, B.; Schiano-Phan, R.; Francis, E. *The Architecture & Engineering of Downdraught Cooling: A Design Sourcebook*, 1st ed.; PHDC Press: London, UK, 2010.

10. Today in Energy: Nearly 90% of U.S. Households Used Air Conditioning in 2020. Available online: https://www.eia.gov/todayinenergy/detail.php?id=52558 (accessed on 3 March 2023).
11. Bryan, B. Water Consumption of Passive and Hybrid Cooling Strategies in Hot Dry Climates. In Proceedings of the 29th National Passive Solar Conference, Portland, OR, USA, 11–14 July 2004.
12. Kang, D.; Strand, R.K. Modeling of simultaneous heat and mass transfer within passive down-draft evaporative cooling (PDEC) towers with spray in FLUENT. *Energy Build.* **2013**, *62*, 196–209. [CrossRef]
13. Ghoulem, M.; El Moueddeb, K.; Nehdi, E.; Zhong, F.; Calautit, J. Analysis of Passive Downdraught Evaporative Cooling Windcatcher for Greenhouses in Hot Climatic Conditions: Parametric Study and Impact of Neighbouring Structures. *Biosyst. Eng.* **2020**, *197*, 105–121. [CrossRef]
14. Givoni, B. Performance of the "shower" cooling tower in different climates. *Renew. Energy* **1997**, *10*, 173–178. [CrossRef]
15. Pearlmutter, D.; Erell, E.; Etzion, Y. A Multi-Stage Down-draft Evaporative Cool Tower for Semi-Enclosed Spaces: Experiments with a Water Spraying System. *Sol. Energy* **2008**, *82*, 430–440. [CrossRef]
16. Calautit, J.K.; Hughes, B.R. A passive cooling wind catcher with heat pipe technology: CFD, wind tunnel and field-test analysis. *Appl. Energy* **2016**, *162*, 460–471. [CrossRef]
17. Duong, S.; Craven, R.; Garner, S.; Idem, S. A novel evaporative cooling tower constructed from an inflatable fabric duct. *Sci. Technol. Built Environ.* **2018**, *24*, 908–918. [CrossRef]
18. Mahon, H.; Friedrich, D.; Hughes, B. Wind tunnel test and numerical study of a multi-sided wind tower with horizontal heat pipes. *Energy* **2022**, *260*, 125118. [CrossRef]
19. Chakraborty, J.; Fonseca, E. Analysis and Evaluation of a Passive Evaporative Cool Tower in conjunction with a Solar Chimney. In Proceedings of the 22nd International Conference on Passive and Low Energy Architecture, Beirut, Lebanon, 13–16 November 2005.
20. Chiesa, G.; Grosso, M. Direct evaporative passive cooling of building. A comparison amid simplified simulation models based on experimental data. *Build. Environ.* **2015**, *94*, 263–272. [CrossRef]
21. Alaidroos, A.; Krarti, M. Experimental validation of a numerical model for ventilated wall cavity with spray evaporative cooling systems for hot and dry climates. *Energy Build.* **2016**, *131*, 207–222. [CrossRef]
22. Zaki, A.; Richards, P.; Sharma, R. Analysis of Airflow inside a Two-Sided Wind Catcher Building. *J. Wind. Eng. Ind. Aerodyn.* **2019**, *190*, 71–82. [CrossRef]
23. Calautit, J.K.; Chaudhry, H.N.; Hughes, B.R.; Sim, L.F. A validated design methodology for a closed-loop subsonic wind tunnel. *J. Wind. Eng. Ind. Aerodyn.* **2014**, *125*, 180–194. [CrossRef]
24. de Almeida, O.; de Miranda, F.C.; Neto, O.F.; Saad, F.G. Low Subsonic Wind Tunnel—Design and Construction. *J. Aerosp. Technol. Manag.* **2018**, *10*, 716. [CrossRef]
25. Al-Hassawi, O.D. Design and Evaluation of Passive Downdraft Cooling Systems: Outcomes from Built Prototypes of Single Stage and Hybrid Downdraft Cooling Towers. *Archit. Sci. Rev.* **2020**, *64*, 17–27. [CrossRef]
26. Sawilowsky, S.S. New Effect Size Rules of Thumb. *J. Mod. Appl. Stat. Methods* **2009**, *10*, 597–599. [CrossRef]